Hindawi
IET Electrical Systems in Transportation
Volume 2024, Article ID 6668174, 12 pages
https://doi.org/10.1049/2024/6668174

Research Article

Inner Resonance and Outer Current Based Control Strategy for Inductive Power Transfer System Used in Wireless Charging for Electric Vehicles

Sooraj Varikkottil,[1] **Febin Daya John Lionel**,[2] **Mohan Krishna Srinivasan**,[3] **Thinagaran Perumal**,[4] **Albert Alexander Stonier**,[5] **Geno Peter**,[6] **Balachennaiah Pagidi**,[7] **and Vivekananda Ganji**[8]

[1]*Tata Elxsi, Trivandrum 695581, India*
[2]*Electric Vehicles Incubation, Testing and Research Center, Vellore Institute of Technology, Chennai 600127, India*
[3]*TCI-IIMB Supply Chain Sustainability Lab, Supply Chain Management Centre, Indian Institute of Management, Bangalore 560076, India*
[4]*Department of Computer Science, Universiti Putra Malaysia, Selangor, Malaysia*
[5]*School of Electrical Engineering, Vellore Institute of Technology, Vellore, Tamil Nadu, India*
[6]*CRISD, School of Engineering and Technology, University of Technology Sarawak, Sarawak, Malaysia*
[7]*Department of Electrical and Electronics Engineering, Annamacharya Institute of Technology and Sciences, Rajampet 516126, India*
[8]*Department of Electrical and Computer Engineering, Debre Tabor University, Amhara, Ethiopia*

Correspondence should be addressed to Vivekananda Ganji; vivekganji@dtu.edu.et

Received 9 September 2023; Revised 20 December 2023; Accepted 20 February 2024; Published 6 March 2024

Academic Editor: Longxing Wu

The wireless charging for electric vehicle is getting popular due to the absence of sophisticated cable connection and associated issues with the actuators in field for connected charging. The major challenges in inductive power transfer (IPT) systems are the control of the resonance converter and synchronisation in communications with the vehicle and power supply. In IPT system, the dynamic nature of load as well as system demands extra care for the existing charging architectures. This work proposes a unique control algorithm to charge the Li-ion battery under coupling coefficient and load variations. The developed control algorithm is validated in MATLAB simscape platform. Further, the control logic is validated using the Texas C2000 Delfino controller in 1 kW IPT system. The developed control logic would ensure proper frequency of operation as well as the constant voltage and constant current control.

1. Introduction

Research in the electric vehicle (EV) has reverberated in recent decades. EVs are one of the permanent transport solutions for the existing greenhouse emissions. In the world land speed record, EV exceeds 1 mile per minute speed during 1899 [1]. The popularity of EVs is increasing day by day replacing the conventional internal combustion (IC) engines used for transportation. The IC engines are less efficient than an electric motor [2]. The fuel economy improvement and reduction of emission were other challenges faced. EV/PHEV vehicles use the battery as a storage device in the system [3]. The schematic of the electric vehicle is portrayed in Figure 1. The electric vehicle comprises of electric motor, inverter module, converter module, battery pack, charging unit, battery management and monitor unit, electronic control unit (ECU), control area network (CAN), etc. [4]. The electric motors such as induction motor, permanent magnet synchronous motor, brushless DC motors are used in EVs. The high-voltage battery bed inside the vehicle is used to power the motor and inverter module. In addition, there will be an auxiliary battery to power the infotainment and the control circuit. The cost of power converters, controllers make the vehicle more expensive than a conventional one. As research progress in this field would result

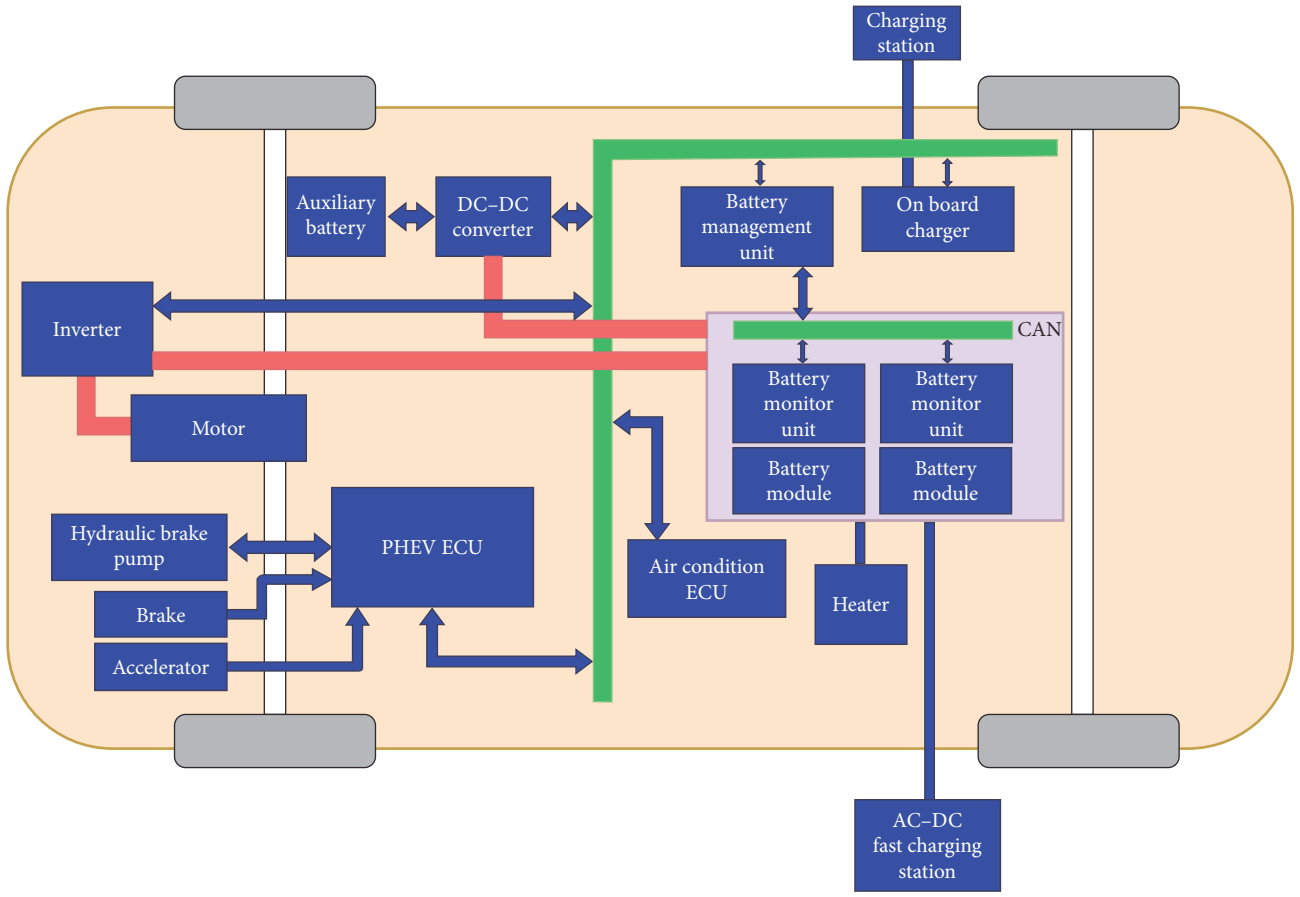

Figure 1: Electric vehicle system.

in a reduction of the cost. The battery of the vehicle is charged from different sources. The available ac supply can be directly fed into the internal on-board charger deployed inside the vehicle. In case of fast charging, high-voltage DC supply is directly fed into the internal integrated DC–DC converter. The chargers are connected to the battery through the power distribution unit (PDU).

The increase in the use of EVs created a huge demand for charging stations [5]. More EVs in the future will increase the demand for the grid. This can be contributed by sustainable energy resources. The integrated-on board charger inside the vehicle communicates with the external electric vehicle supply equipment (EVSE) system through control pilot for hand shaking. Thereafter, the power is drawn from the source through EVSE. The major constraint of the electric vehicle is the charging limitations. The availability of power and opportunity of charging are the two key features that decide the range of vehicles over a single charge [6, 7]. The vehicle is charged through connected cables. However, the sophisticated cable reduces the ease of access to the charging ports. There is more probability to get an electric shock from the high-voltage supply from the broken cables. SAE J1772 standards are recommended for wired charging applications [8].

The sophisticated wired connectors limit the freedom of an object to be powered [9]. The time-varying supply produces time-varying electromagnetic field across space. The load available at the receiving end gets the power from the secondary receiver [10, 11]. This will increase the freedom of movement of the object subjected to charge. The WPT technique is mainly classified into the near field and far-field. In near-field category, inductive power transfer (IPT) is achieved through resonance IPT and capacitive coupling [12, 13]. In case of far-field regions, microwaves and light waves are used. The frequency of operation for the WPT system varies from kHz to MHz range depending upon the technique used [14]. IPT is widely used for induction heating and induction stovetops, etc.

Resonance enhanced IPT is used for portable device charging (Qi standard), electric vehicle, biomedical implants, trains, RFID, MAGLEV, etc. IPT is an effective way of powering the near field systems (the one wavelength (λ) of the antenna is considered as near field and nonradiative region). IPT technique is conceptually coined using Faraday's electromagnetic induction as well as Ampere circuital law [15, 16]. There are two coaxial coils made up of copper placed in the medium of air. The ferrite spokes are deployed under the coil [17]. The high current flowing through the coil with high frequency increases the amount of power transferred to the isolated circuit. Figure 2 shows the generalised block diagram for the IPT system. The system comprises of input EMI filter followed by rectifier, filter, high-frequency inverter, coils, and other secondary circuits [18].

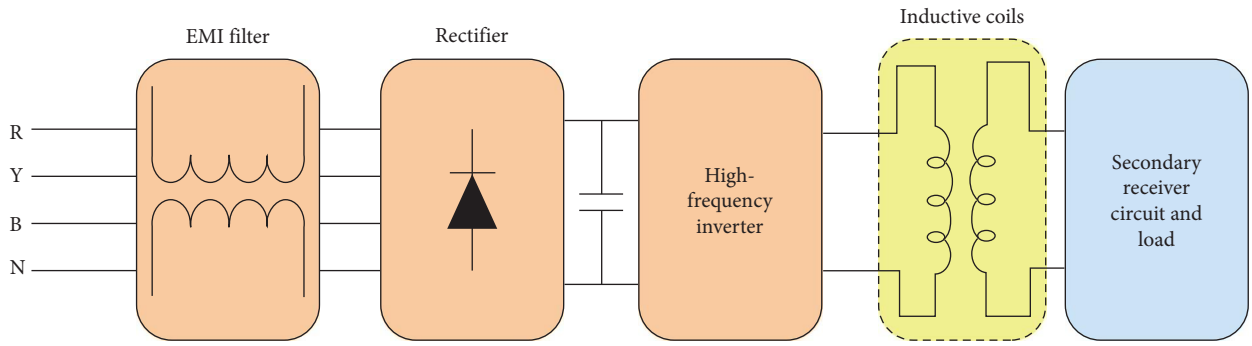

FIGURE 2: Generalised block diagram of IPT system.

The closed-loop control of the IPT system is essential to meet the resonance condition and charging profile [19, 20]. The different parameter variations in the IPT system bring the operating region out of resonance condition. This would eventually reduce the power transfer efficiency. The IPT system is connected to the HV battery bed. Most of the electric vehicle uses Li-ion battery due to high energy and power density [21, 22]. The Li-ion battery needs to be charged using CCCV control. The battery management system (BMS) gives the information regarding the required charging current. In addition, the BMS balances the cell and gives information regarding the state of charge (SOC) [23]. Depending upon the SOC, the charging current is decided. The battery bed inside a vehicle comprises of series and parallel connected battery cells. Any sort of battery charger such as on-board or fast charger is connected to the battery through the PDU. This is to ensure the safety of the battery. Each cell can be represented as RC based equivalent circuit. The Li-ion cells have very less self-discharge [24]. The conventional LCL based IPT system as well as proposed high gain and compact IPT systems are working as per the resonance architecture. In most cases,

(1) Li-ion battery needs to be charged with less current ripple;
(2) the rectified PFC circuit would have low-frequency current ripple and the high-frequency resonance operation injects more high-frequency current ripple in the charging current output.

The presence of low-frequency current ripple in the converter output voltage is reduced by the dedicated faster control circuit. In most of the practical applications, the output power will not remain constant due to the coupling coefficient and load variations. In the literature, parity time symmetry front end DC–DC converter is proposed for series–series compensated IPT system to stabilise the output power. The proposed method comprises of the load resistance identification followed by the output power estimation. Similarly, a dedicated control strategy is used in a 3.3 kW IPT system with LCC compensated network to increase the power transfer efficiency by 3.75%. In case of the swiftness of the transient response of the IPT system, a combination of once cycle control and proportional differential control is proposed by Shi et al. [25]. A unique control algorithm by providing importance to the user demand gives more opportunity in customised charging scenarios. In which, the optimal charging trajectory is made from the nominal battery model. In addition, the outer SOC tracking based charging control followed by the inner fuzzy PI based control is implemented in this circuit [26].

The resonance frequency selection for IPT system irrespective to the compensation topologies are essential to attain high-power transfer efficiency. Hence, an estimation of resonance frequency under the load and coupling coefficient variation is addressed in the manuscript. Therefore, it is necessary to develop a suitable control strategy for the IPT system to meet the desired response. In this paper,

(1) the control strategy for the IPT system is developed to meet the efficiency and charging profile over the coupling coefficient and load variations;
(2) the state-space model of the equivalent circuit gives the information regarding the stability and control freedom. It also provides information regarding the resonance frequency;
(3) the perturbation of different parameters over resonance frequency is studied in detail. The respective simulation and experimental studies are done;
(4) in addition, a generalised control algorithm is developed to control the frequency, pulse position, and pulse width.

In comparison with the existing control strategies [27, 28], the proposed control strategy is critical in estimating the mutual inductance and calculating the operating frequency. The error in approximation in elliptical integral of first and second kind given Neumann's formula in Equation (3) decides the accuracy in mutual inductance theoretically. The practical measurement of voltage across the capacitance and current to the load is an input to the mutual inductance estimation. The advantage of the proposed control strategy over the existing control strategy is that even in absence of voltage and current measurement, if the physical dimensions of inductive coils and misalignments are known, the mutual inductances can be estimated. Combining the Neumann's formula and resonance conditions is the unique control strategy used in the IPT system.

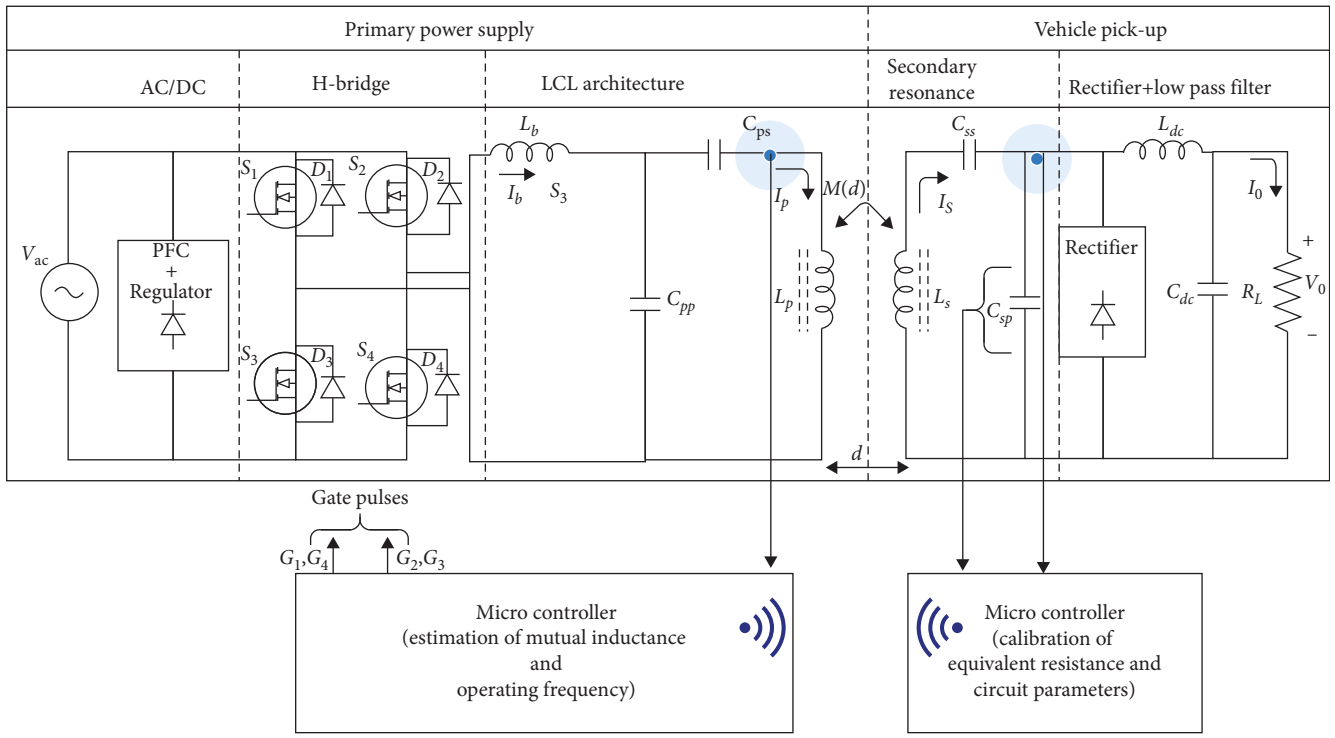

FIGURE 3: LCL based IPT system with closed loop.

The future studies need to improve the accuracy of the estimation and bring the optimised performance while measuring the significant misalignments. The studies should also focus on the external interventions that affects the measurement of voltage and currents and estimation.

The organisation of the paper is as follows: Section 1 emphasises the background and motivation behind the proposed work, Section 2 gives the mathematical foundation and details the proposed control logic and algorithm, Section 3 presents the validation in simulation and experimental platforms along with result analysis and discussion. This is followed by conclusion.

2. State Space Model of Equivalent Circuit

The conventional LCL based IPT system is considered for closed-loop study. The circuit diagram of closed-loop control of the IPT system is shown in Figure 3. The current through the bridge rectifier and voltage across the secondary parallel capacitor is sensed. The equivalent circuit of the LCL based IPT system is shown in Figure 4. The sensed current and voltage data are transferred to the primary side. The TI Delfino C2000 controller is used as controller.

The state variables for the secondary circuit are the current through the equivalent secondary inductance (L_{seq}) and the voltage across the secondary parallel capacitor (C_{sp}). The corresponding secondary decoupled circuit is shown in Figure 4(a). The output variable is the secondary voltage across capacitor C_{sp}.

L_{seq} is the equivalent secondary inductance made from combining the elements L_s and C_{ss} shown in Figure 4. This is mathematically expressed as follows:

$$L_{\text{seq}} = L_s - \frac{1}{\omega^2 C_{ss}}, \tag{1}$$

where L_s is the secondary coil self-inductance and C_{ss} is the capacitance added to compensate the leakage flux created due to the large distance between the coil. The capacitance C_{sp} is resonating with the inductance.

$$\begin{bmatrix} \frac{dx_1}{dt} \\ \frac{dx_2}{dt} \end{bmatrix} = \begin{bmatrix} 0 & \frac{-1}{L_{\text{seq}}} \\ \frac{1}{C_{sp}} & \frac{-1}{R_{eq} C_{sp}} \end{bmatrix} \begin{bmatrix} x_1 \\ x_2 \end{bmatrix} + \begin{bmatrix} \frac{1}{L_{\text{seq}}} \\ 0 \end{bmatrix} V_{oc}, \tag{2}$$

$$y = \begin{bmatrix} 0 & 1 \end{bmatrix} \begin{bmatrix} x_1 \\ x_2 \end{bmatrix}, \tag{3}$$

where x_1 is the current through the inductor L_{seq} and x_2 is the voltage across the capacitor C_{sp}. The output matrix represents the voltage measured across the equivalent resistance made from the uncontrolled rectifier and load by considering the fundamental harmonic approximation.

Similarly, the approximated secondary circuit elements are referred to primary and formed and the equivalent circuit is shown in Figure 4(b). The current through the equivalent primary inductor, voltage across primary parallel capacitor and current through bridge inductor are the state variables. The corresponding state–space model is shown below.

The state variable x_3 is the current through the bridge inductor L_b. x_4 is the voltage across the capacitor C_{pp}. x_5 is

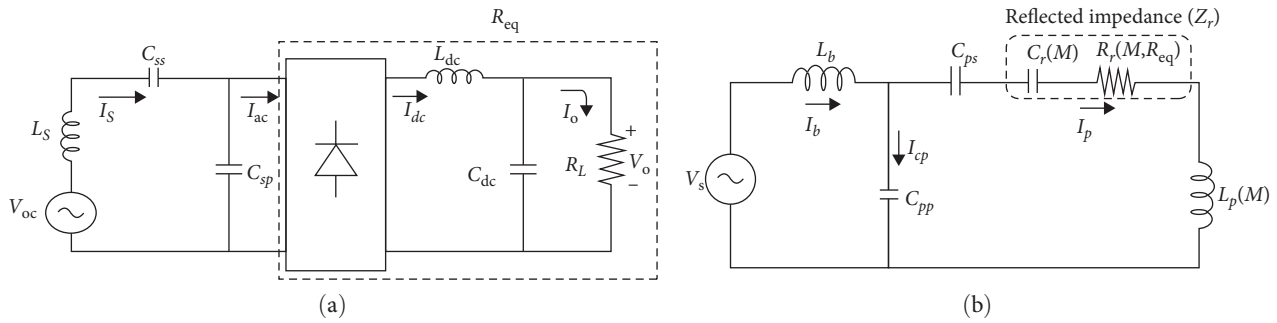

FIGURE 4: Equivalent circuits: (a) secondary decoupled equivalent circuit and (b) primary equivalent circuit.

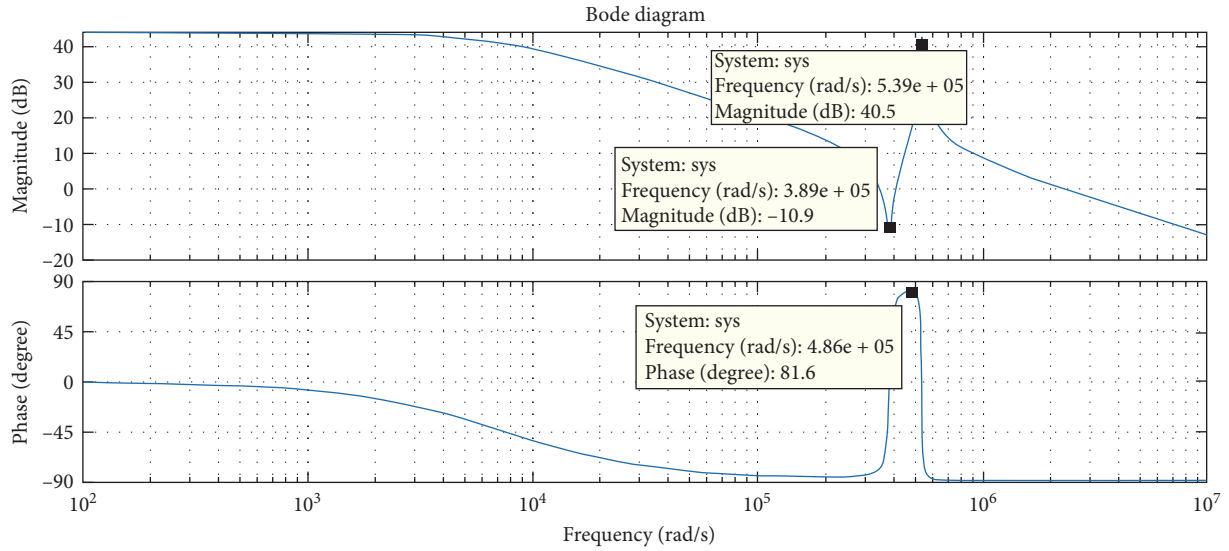

FIGURE 5: Bode plot as current I_b as output.

the current through the equivalent inductor L_{peq}.

$$\begin{bmatrix} \frac{dx_3}{dt} \\ \frac{dx_4}{dt} \\ \frac{dx_5}{dt} \end{bmatrix} = \begin{bmatrix} 0 & \frac{1}{L_b} & 0 \\ \frac{1}{C_{pp}} & 0 & \frac{-1}{C_{pp}} \\ 0 & \frac{1}{L_{peq}} & \frac{-R_r}{L_{peq}} \end{bmatrix} \begin{bmatrix} x_3 \\ x_4 \\ x_5 \end{bmatrix} + \begin{bmatrix} \frac{1}{L_b} \\ 0 \\ 0 \end{bmatrix} V_s, \quad (4)$$

$$\boldsymbol{y} = \begin{bmatrix} 0 & 0 & 1 \end{bmatrix} \begin{bmatrix} x_3 \\ x_4 \\ x_5 \end{bmatrix}. \quad (5)$$

Further, the bode plot of the state space model is taken to understand the gain and bandwidth details. The current I_b flowing through bridge inductor is limited by the inductor as well as parallel resonance condition. The corresponding bode plot with current I_b as output variable is shown in Figure 5. The capacitor C_{pp} is resonated with primary equivalent inductance L_{peq}. Since the bridge current drawn by the circuit is minimum to meet the load at that time, the conduction loss through the switches will be minimum. This region of operation can be well identified with a bode plot. Similarly, Figure 6 shows the bode plot with the primary current as output. The primary current drawn during resonance condition would be very high. This eventually create more open-circuit voltage at the secondary side.

2.1. Estimation of Mutual Inductance. It is estimated from sensing the circuit parameters. In addition, from the physical dimensions of the inductive coil, misalignment and mutual inductance are computed. According to the change in dimensions, the mutual inductance will vary. However, the mutual inductance estimated from the sensed current and voltage parameter is applicable to all kinds of coil dimensions. Both methods are combined to get information regarding the unknown parameters.

2.1.1. Computation of Mutual Inductance. The mutual inductance between the primary and secondary coil is computed from the Neumann's formula of approximations.

The primary coil is embedded in the ground and part of the power supply equipment system. The secondary pickup coil is placed in the vehicle. The secondary pickup coil gets misaligned when the car is not parked in line with the coil

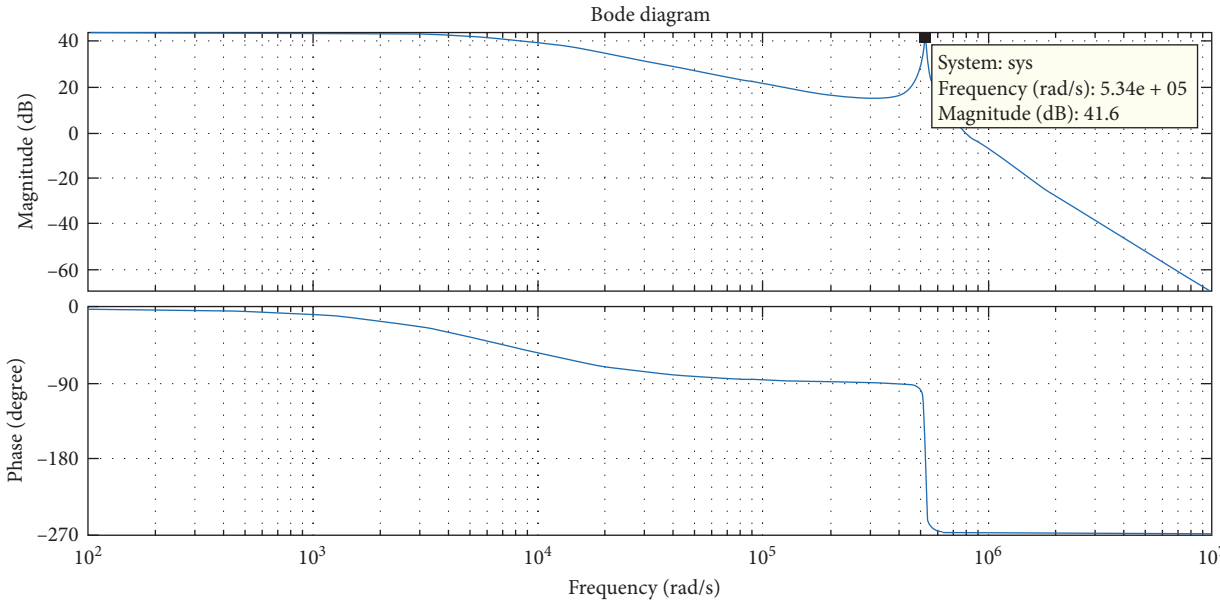

FIGURE 6: Bode plot current I_p as output.

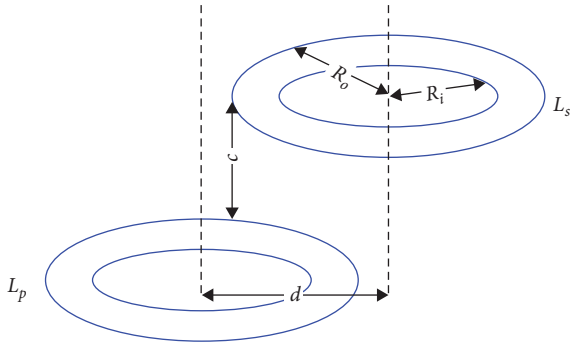

FIGURE 7: Misaligned IPT coils.

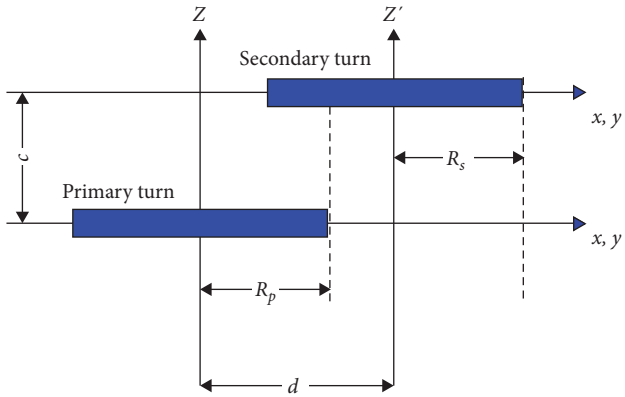

FIGURE 8: Primary and secondary coil turns.

alignment. A typical example is represented as image in Figure 7. Each turn in primary and secondary coils are represented in Figure 8.

The R_p is the radius of the primary turn and R_s is the radius of the secondary turn. Where 'd' is the distance between the centre axis of the coils. k is the modulus where $0 < k^2 < 1$.

$$M_{ij} = \frac{\mu_0}{\pi} \int_0^{\pi} \frac{\left(1 - \frac{d}{R_s}\cos\emptyset\right)}{\sqrt{V^3}} d\emptyset, \tag{6}$$

where i is the primary turn and j is the secondary turn. Similarly, the term V is represented as follows:

$$V = \sqrt{1 + \frac{d^2}{R_s^2} - 2\frac{d}{R_s}\cos\emptyset}. \tag{7}$$

The function $\Psi(k)$ is the function of elliptical integral first ($K(k)$) and second ($E(k)$) kind as follows:

$$\varphi(k) = \left(\frac{2}{k} - k\right)K(k) - \frac{2}{k}E(k). \tag{8}$$

The elliptical integral of first kind is written as follows:

$$K(m) = \int_0^{\pi} \sqrt{\frac{1}{1 - m\sin^2\theta}} d\theta, \tag{9}$$

$$E(m) = \int_0^{\pi} \sqrt{1 - m\sin^2\theta} d\theta. \tag{10}$$

The elliptical integral of first kind and second kind is represented in Figure 9. When the mutual inductance is getting increased then the difference between the elliptical integral first kind and second kind is getting increased.

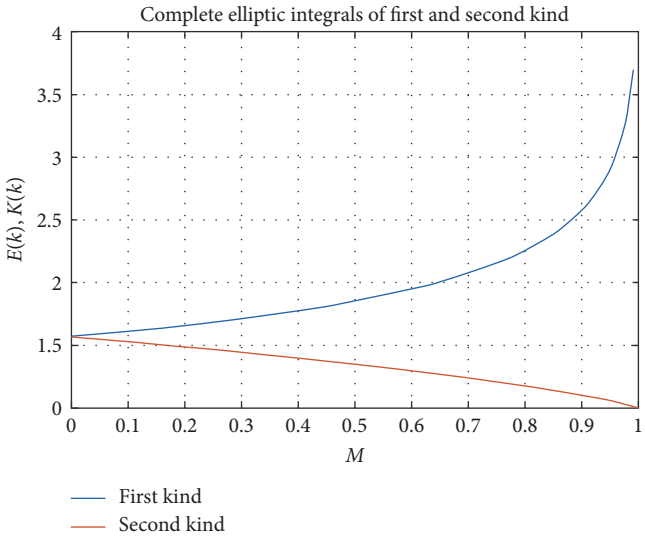

FIGURE 9: Elliptical integral of first kind and second kind.

2.1.2. Estimation of Mutual Inductance from Circuit Parameter Identification. From the fundamental voltage across the capacitor C_{sp} and current through the diode bridge (I_{db}) the equivalent resistance is computed. This is similar to the approximated equivalent resistance from load as follows:

$$R_{eq} = \frac{V_{Csp1}}{I_{db1}}. \tag{11}$$

Now, the circuit becomes linear at the secondary side. Applying the Kirchhoff current law (KCL),

$$\overrightarrow{I_s} = \overrightarrow{I_{Csp}} + \overrightarrow{I_{db}}. \tag{12}$$

Similarly, the open-circuit voltage in terms of primary current and mutual inductance is written as follows:

$$V_{oc} = j\omega M I_p. \tag{13}$$

The mutual inductance in terms of other circuit parameters is written as follows:

$$M = \frac{I_s \omega L_{\text{seq}} + I_{Csp}\omega C_{sp}}{\omega I_p}. \tag{14}$$

In addition, the secondary inductive coil is embedded inside the vehicle. The inductance of the secondary pickup coil can be measured using the test pulse. The information is useful to determine the open-circuit voltage without the primary current (I_p). The parameter such as secondary current (I_s), secondary parallel capacitor (C_{sp}), and frequency (ω) are known. Further, from the primary side current measurement (I_p) is also obtained. Thereafter, the mutual inductance is calculated using Equation (11). The estimated mutual inductance from current and voltage measurement and computed mutual inductance using Neumann's formula exactly determine the position of the coil.

2.1.3. Selection of Operating Frequency. The operating frequency of the proposed converter is selected as follows:

$$\omega_0 = \frac{1}{\sqrt{L_{\text{peq}} C_{pp}}}. \tag{15}$$

The resonance frequency of the system is selected as the operating frequency. The equivalent primary inductance is written as follows:

$$L_{\text{peq}} = L_p - \frac{1}{\omega^2 C_{ps}} - \frac{1}{\omega^2 C_r}. \tag{16}$$

The reflected capacitor is written in terms of mutual inductance.

$$C_r\left(M, R_{eq}\right) = \frac{R_{eq}^2\left(\omega^2 C_{sp} L_{\text{seq}} - 1\right)^2 + \left(\omega L_{\text{seq}}\right)^2}{\left(\omega^4 M^2\right)\left[C_{sp} R_{eq}^2\left(\omega^2 C_{sp} L_{\text{seq}} - 1\right) + L_{\text{seq}}\right]}. \tag{17}$$

The mutual inductance is computed corresponds to the misalignment of the inductive coil. Hence, the operating frequency is selected according to the misalignment of the pickup coil with respect to the primary coil.

2.2. Proposed Control Logic and Algorithm. The inner resonance and outer current control logic block diagram is shown in Figure 10. The sensed current and voltage is calibrated and transmitted through the RF medium. Since the primary and secondary pickup coil is near, RF-based signal transmission is adopted. The received RF signal shares the information regarding the corresponding voltage and current. Further, the calibrated current value shows the actual measured current and compared with the reference current value. The reference current is decided according to the requirement of charging current. The charging current is high when the SOC is low.

Meanwhile, the calibrated voltage is compared with the reference voltage. The reference voltage is decided by the constant voltage (CV) limit. The proposed algorithm is shown in Figure 11. The pulse width, position, and frequency are adjusted as per the logic developed. The resonance frequency is selected according to the condition of resonance. There are two reference voltages fixed to identify the CC and CV points. According to the specifications of the battery, these reference voltages are fixed. The measured battery current is compared with the current reference. Depending upon the error, the pulse width modulation (PWM) duty is adjusted. During constant current mode, the PWM duty is adjusted to maintain a fixed current magnitude. The current

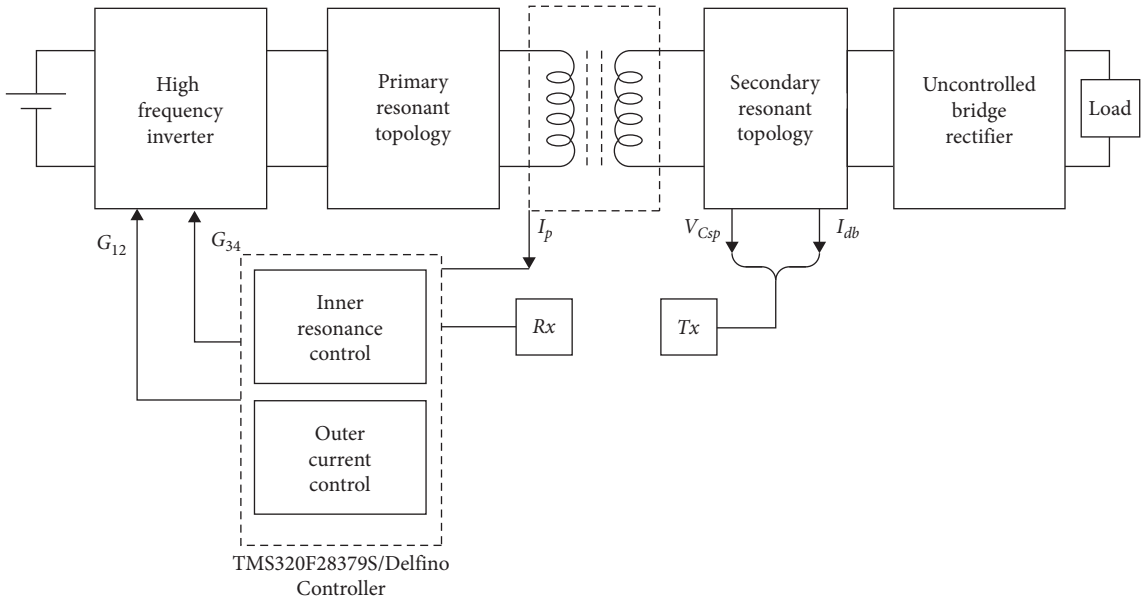

FIGURE 10: Inner resonance and outer current control.

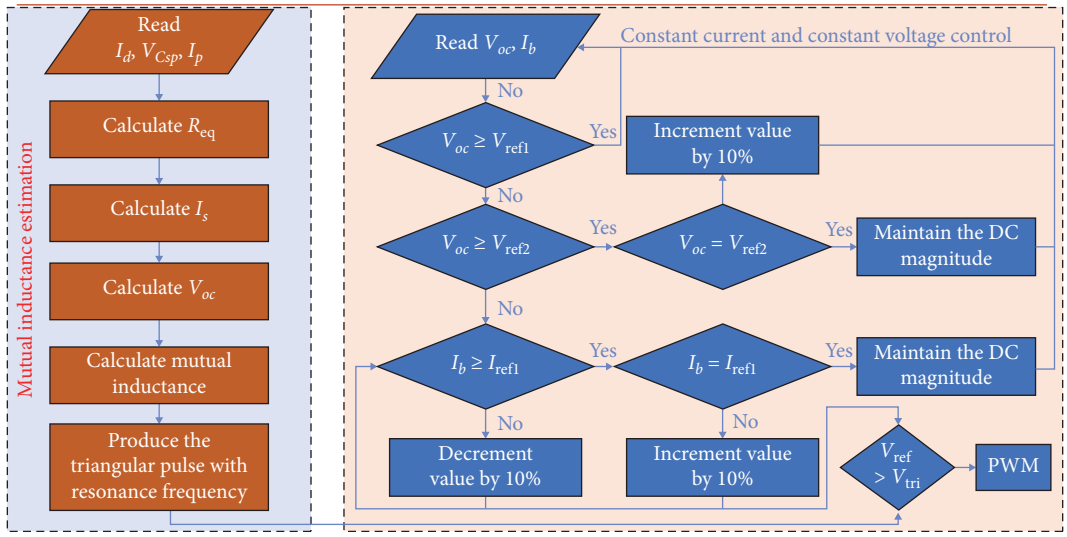

FIGURE 11: Flowchart of the algorithm.

tolerance limit is decided according to the desired current ripple at the charging current. Operating frequency verses the coupling coefficient is shown in Figure 12. This shows the optimised frequency selection for the resonance operation.

Generally, the charger inside the vehicle is a slave to the Vehicle supervisory unit (or) power train control module. Hence, the current reference value from battery management system given to the vehicle supervisory unit and charge power available from charger point or EVSE is communicated to vehicle supervisory unit over CAN. V_{ref1}, V_{ref2}, I_{ref1}, and I_{ref2} are calculated from the power request from the vehicle supervisory unit. V_{ref1} and V_{ref2} are derived from the SOC of the battery and the voltage setpoint request from the master. I_{ref1} and I_{ref2} are calculated from the charge power request and voltage references.

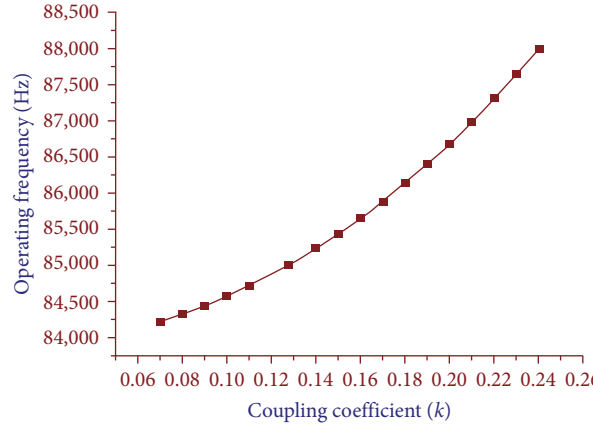

FIGURE 12: Operating frequency vs. coupling coefficients.

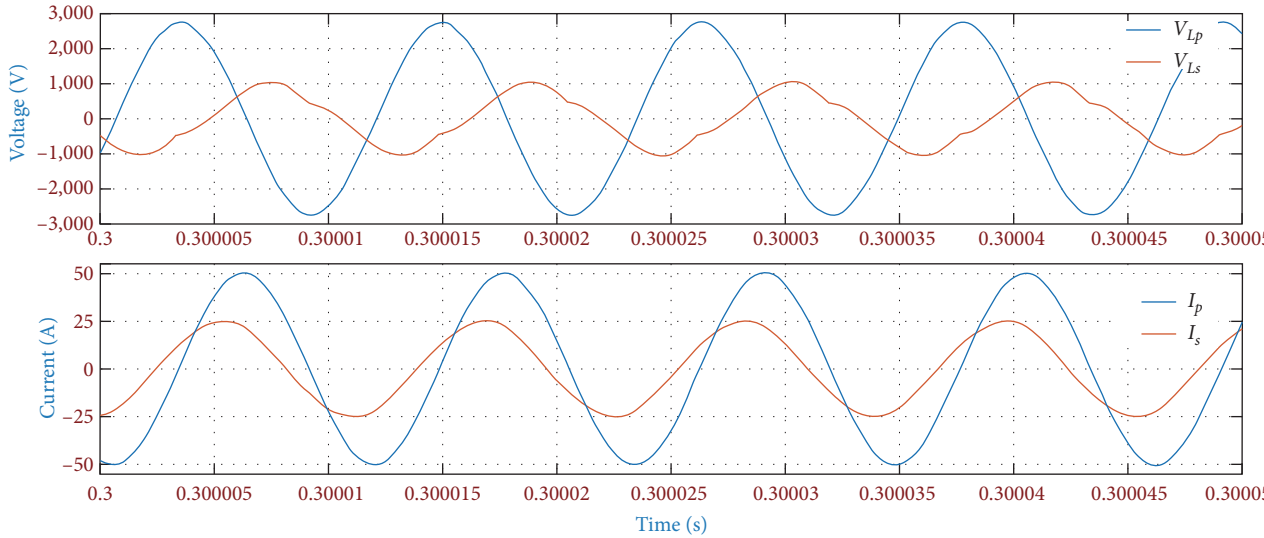

Figure 13: Voltage and current waveform of primary and secondary coils.

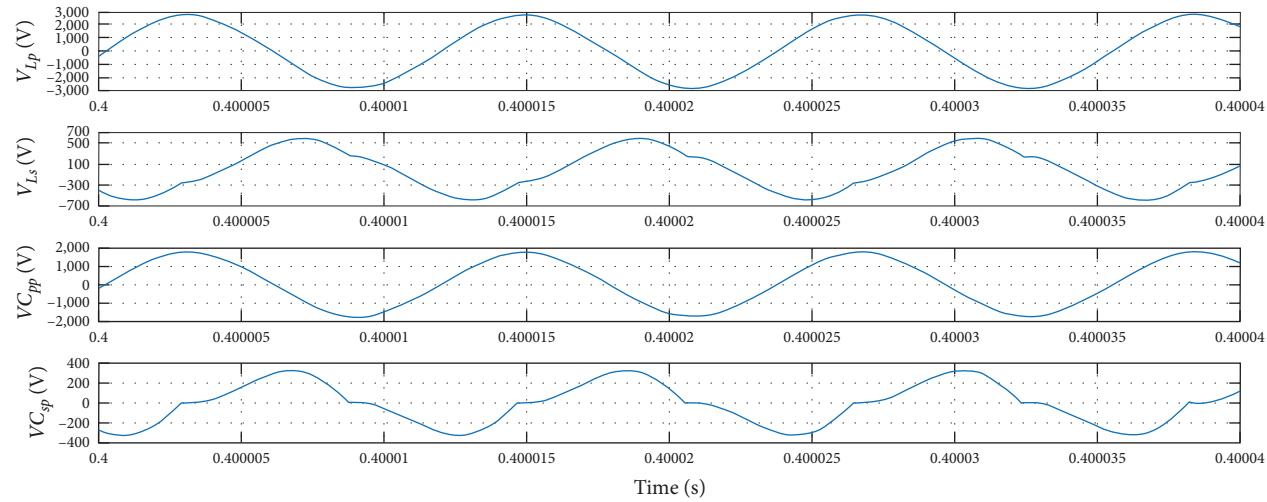

Figure 14: Voltage across various circuit elements.

3. Implementation and Validation

The proposed control algorithm and the control logic needs to be evaluated in simulation and experimental studies. In view of that, a control logic is built in MATLAB platform and validated numerically as well as experimentally.

3.1. Simulation Studies. A closed-loop control of the IPT system with the proposed control logic is implemented in the MATLAB simulation platform. In case of LCL circuit, the significant amount of output voltage is controlled by adjusting the frequency of operation. The pulse width is also adjusted for minimal changes. Further, the developed IPT system is simulated with the same environment. The steady-state waveforms of the LCL based IPT system is taken. The voltage and current waveforms of the primary and secondary coil is shown in Figure 13. According to the frequency of operation, the primary current varies. This in turn changes the primary and secondary waveforms.

The voltage across various circuit elements is shown in Figure 14. Similarly, current through various circuit elements are shown in Figure 15.

The steady-state voltage and current waveform shows a stable operation. Further, the constant voltage and current operation the developed algorithm is built-in MATLAB platform.

3.1.1. Constant Current and Constant Voltage Control. According to the SOC of the battery, the constant voltage and constant current control are developed. Figure 12 shows the constant current control. The dynamic changes in load lead to variation in current. The current reference is decided in accordance with the desired charging current under constant current operation. The waveform reaches to steady state after 0.2 s. Thereafter, the

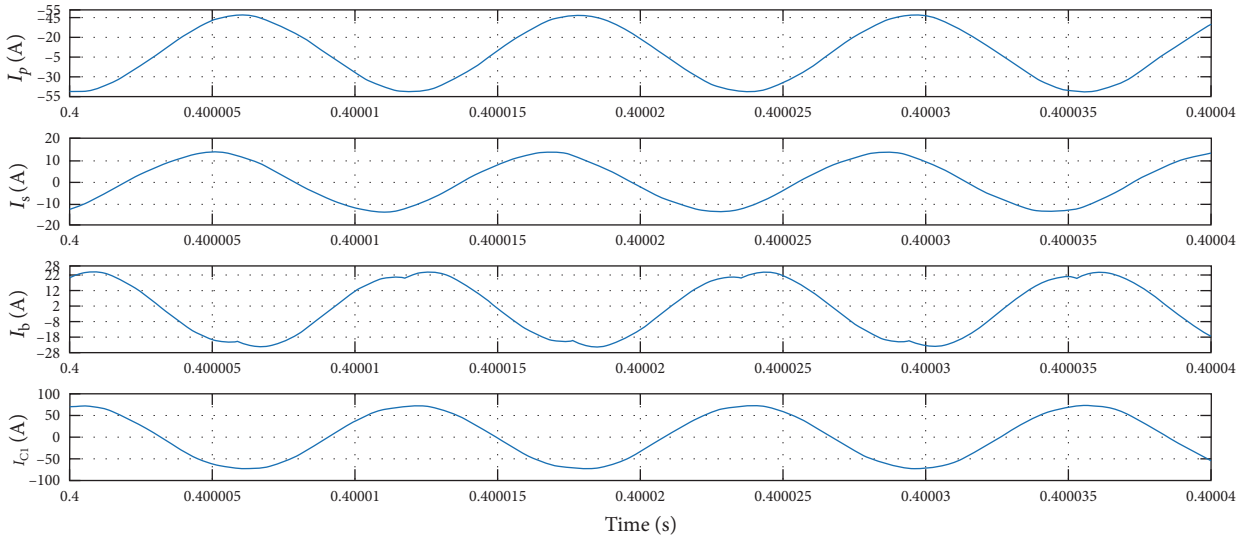

FIGURE 15: Current through various circuit elements.

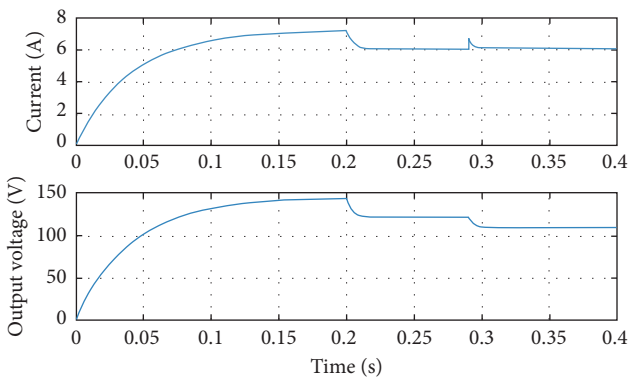

FIGURE 16: Constant current control.

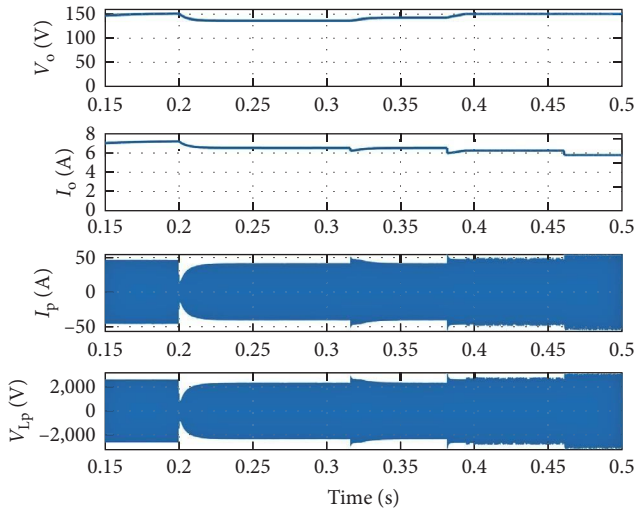

FIGURE 17: Constant voltage and constant current control.

FIGURE 18: Experimental setup and prototype.

change in effective equivalent resistance leads to a change in charging current. The charging current is maintained constant through variable voltage and closed-loop current control. Similarly, the constant current and constant voltage control are shown in Figure 16. The SOC of the battery reaching after a certain limit, the mode of charging is changed to constant voltage control. Meanwhile, the charging current reduces while there is progress in SOC. This eventually shows the typical charging profile of the Li-ion batteries. The resonance frequency is adjusted in accordance to the misalignment of pickup coil. There is a small spike in current value after reaching 0.3 s, when the voltage transitions occur. This is due to the time in estimations in mutual inductance after measuring the primary current. The estimation time to be reduced and the controller to be optimised in further iterations.

3.1.2. Simulation Results for Selection of Resonance Frequency. The gate pulses with a different frequency as well as different duty ratios is used to control the desired output response. The resonance frequency is adjusted to maintain high-power transfer efficiency. The change in the load will not affect the resonance frequency. However, the frequency of operation can adjust the output voltage. The main impact in resonance frequency is due to a change in mutual inductance. In view of that, the resonance frequency should match the operating frequency of the system. The pulse width and pulse position are decided by the control logic adopted. In case of compact high-efficient IPT system pulse position-based control is required. However, the condition of resonance in terms of circuit parameters are different. In addition, according to

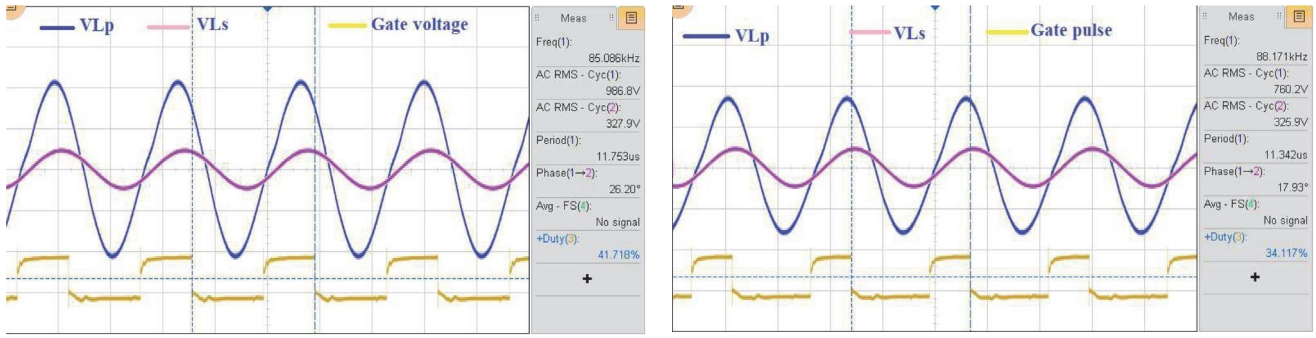

(a) (b)

FIGURE 19: Experimental waveforms. (a) Voltages V_{Lp}, V_{Ls} and gate pulses at 42% and (b) voltages V_{Lp}, V_{Ls} and gate pulses at 34%.

the circuit and mode of operation, the resonance will vary. Hence, as per the guidelines, this control logic can be applied to any such IPT systems. The increase in the magnitude of voltage and current according to the resonance frequency is shown in Figure 17.

3.1.3. Experimental Studies. The control logic is tested in the built experimental prototype. C2000 Delfino controller is used as the main controller. The experimental prototype of 1 kW with closed loop control is shown in Figure 18. The ACS712 hall effect current sensor is used to measure the charging current. Thereafter, the measured current is given to the ADC of Delfino controller and calibrated. Similarly, the voltage across the capacitor C_{sp} is sensed using ZMPT101B. Further, ADC of the controller reads the voltage and current values from the sensor output. The steady state equivalent resistance is calculated from the fundamental magnitude of the measured voltage to the fundamental magnitude of the measured current. Predefined circuit parameters are declared as constant in the programme. The primary current through the inductive coil is also measured in this regard. The entire control logic is built-in MATLAB embedded programming platform along with the help of a code compressor studio. The Delfino controller is interfaced with the PC where MATLAB is installed. The simulation time is matched with the hardware execution time and retrieved the live readings from the ADCs. Further, the processed value is given to the converter as a gate pulse.

The isolated gate driver is used to drive the higher side converters. Silicon labs isolated gate drivers are used to drive the higher side switches. An auxiliary power supply is made to the driver circuit for sufficient energy to operate. Further, the experiments are conducted under variations in misalignment and changes in load. The obtained waveforms from the experiment is shown in Figure 19. The waveform at different duty ratio and frequency are taken in experimental studies. Primary and secondary voltages at 42% duty ratio at 85 kHz are shown in Figure 19(a). Similarly, primary and secondary voltages at 34% duty ratio at 88.171 kHz are shown in Figure 19(b). Each curve shows the way at which the voltages are controlled. Both curves are taken at two different loads and misalignment.

A mathematical model-based approach may inaccurate to meet the exact resonance in the system. A normal PI control with the constant voltage and constant current also is insufficient to meet the desired response. In this proposed technique, since the voltage and current sensor measure each voltage and current values the calculation of impedance will be accurate. In addition, even if there is change in values of the circuit parameters the algorithm is capable enough to capture the changes.

4. Conclusion

The proposed control strategy for IPT system in this paper under misalignment of pickup coil with respect to the primary coil is useful for where there is a parking constraint to the vehicles. The entire control strategy can be comprehended to two parts. The part 1 is the estimation of mutual inductance and part 2 is computing the resonance frequency to generate the pulses for gate drivers. The mutual inductance is computed using Neumann's formula of approximation from the dimension and position of inductive coils. Similarly, the mutual inductance is estimated from measuring the circuit parameters and calculation. Both methods are combined to form a unique control algorithm. The resonance frequency corresponds to the misalignment and load variation is identified by estimating the mutual inductance. The control algorithm is simulated and validated in the MATLAB simulation platform. Further, the developed control algorithm is built-in embedded MATLAB platform and build to the respective controller. The TI C2000 Delfino control launchpad is used to evaluate the control algorithm. Hall effect current sensor with high accuracy and sensitivity is used to measure the current. The use of silicon lab drivers for the experimental setup improved the gate voltage profiles. The developed control algorithm is tested in a conventional LCL based IPT system.

Data Availability

The required data can be obtained from the corresponding author upon an email request.

Conflicts of Interest

The authors declare that they have no conflicts of interest.

Acknowledgments

This research was funded by the University Research Grant, Grant/Award Number: UTS/3/2022/06 and the Centre for Research of Innovation and Sustainable Development (CRISD) of University of Technology Sarawak, Malaysia.

References

[1] Q. Ren, D. Crolla, and A. Morris, "Effect of transmission design on electric vehicle (EV) performance," in *2009 IEEE Vehicle Power and Propulsion Conference*, IEEE, 2009.

[2] Q. Ni, L. Quan, X. Zhu, Y. Du, and K. Shi, "Energy management control strategy for plug-in hybrid electric vehicle with brushless dual-rotor flux-switching permanent magnet motor," in *2015 18th International Conference on Electrical Machines and Systems (ICEMS)*, IEEE, 2015.

[3] V. Sreedhar, "Plug-in hybrid electric vehicles with full performance," in *2006 IEEE Conference on Electric and Hybrid Vehicles, IEEE*, 2006.

[4] B. Frieske, M. Kloetzke, and F. Mauser, "Trends in vehicle concept and key technology development for hybrid and battery electric vehicles," in *2013 World Electric Vehicle Symposium and Exhibition (EVS27)*, IEEE, 2013.

[5] G. Waltrich, M. A. M. Hendrix, and J. L. Duarte, "Three-phase bidirectional DC/DC converter with six inverter legs in parallel for EV applications," *IEEE Transactions on Industrial Electronics*, vol. 63, no. 3, pp. 1372–1384, 2016.

[6] J.-Y. Lee, "An EL capacitorless EV on-board charger using harmonic modulation technique," *IEEE Transactions on Industrial Electronics*, vol. 61, no. 4, pp. 1784–1787, 2014.

[7] M. Yilmaz and P. T. Krein, "Review of battery charger topologies, charging power levels, and infrastructure for plug-in electric and hybrid vehicles," *IEEE Transactions on Power Electronics*, vol. 28, no. 5, pp. 2151–2169, 2013.

[8] A. Zahedmanesh, D. Sutanto, and K. M. Muttaqi, "Analyzing the impacts of charging plug-in electric vehicles in low voltage distribution networks: a case study of utilization of droop charging control system based on the SAE j1772 standard," in *2017 Australasian Universities Power Engineering Conference (AUPEC)*, IEEE, 2017.

[9] M. Li, G. Yao, L. Zhou, and Z. Yin, "Harmonic analysis of bidirectional LCL-IPT system," in *2016 IEEE 2nd Annual Southern Power Electronics Conference (SPEC)*, IEEE, 2016.

[10] J.-H. Choi, S.-K. Yeo, S. Park, J.-S. Lee, and G.-H. Cho, "Resonant regulating rectifiers (3R) operating for 6.78 MHz resonant wireless power transfer (RWPT)," *IEEE Journal of Solid-State Circuits*, vol. 48, no. 12, pp. 2989–3001, 2013.

[11] Y. Zhang, T. Lu, Z. Zhao, F. He, K. Chen, and L. Yuan, "Selective wireless power transfer to multiple loads using receivers of different resonant frequencies," *IEEE Transactions on Power Electronics*, vol. 30, no. 11, pp. 6001–6005, 2015.

[12] H. Funato, H. Kobayashi, and T. Kitabayashi, "Analysis of transfer power of capacitive power transfer system," in *2013 IEEE 10th International Conference on Power Electronics and Drive Systems (PEDS)*, IEEE, 2013.

[13] B. Minnaert and N. Stevens, "Maximizing the power transfer for a mixed inductive and capacitive wireless power transfer system," in *2018 IEEE Wireless Power Transfer Conference (WPTC)*, IEEE, 2018.

[14] M. Liu, M. Fu, and C. Ma, "Parameter design for a 6.78-MHz wireless power transfer system based on analytical derivation of class E current-driven rectifier," *IEEE Transactions on Power Electronics*, vol. 31, no. 6, pp. 4280–4291, 2016.

[15] J. T. Boys and G. A. Covic, "The inductive power transfer story at the University of Auckland," *IEEE Circuits and Systems Magazine*, vol. 15, no. 2, pp. 6–27, 2015.

[16] G. A. Covic and J. T. Boys, "Inductive power transfer," *Proceedings of the IEEE*, vol. 101, no. 6, pp. 1276–1289, 2013.

[17] W. Peng and Z. Chen, "Enhanced planar wireless power transfer systems with ferrite material," in *2018 IEEE Wireless Power Transfer Conference (WPTC)*, IEEE, 2018.

[18] J. Dai and D. C. Ludois, "A survey of wireless power transfer and a critical comparison of inductive and capacitive coupling for small gap applications," *IEEE Transactions on Power Electronics*, vol. 30, no. 11, pp. 6017–6029, 2015.

[19] C. Xia, Q. Sun, X. Li, and A. P. Hu, "Robust μ-synthesis control of dual LCL type IPT system considering load and mutual inductance uncertainty," *IEEE Access*, vol. 7, pp. 72770–72782, 2019.

[20] Q. Deng, Z. Wang, C. Chen et al., "Modeling and control of inductive power transfer system supplied by multiphase phase-controlled inverter," *IEEE Transactions on Power Electronics*, vol. 34, no. 9, pp. 9303–9315, 2019.

[21] C.-H. Kim, M.-Y. Kim, and G.-W. Moon, "A modularized charge equalizer using a battery monitoring IC for series-connected Li-ion battery strings in electric vehicles," *IEEE Transactions on Power Electronics*, vol. 28, no. 8, pp. 3779–3787, 2013.

[22] A. A. Hussein, "Capacity fade estimation in electric vehicle Li-ion batteries using artificial neural networks," *IEEE Transactions on Industry Applications*, vol. 51, no. 3, pp. 2321–2330, 2015.

[23] J. S. Goud, K. R., K. R., and B. Singh, "Low frequency ripple charging of Li-ion battery using bidirectional zeta DC-DC converter to improve charge transfer efficiency," in *2018 IEEE 7th International Conference on Power and Energy (PECon)*, pp. 62–66, IEEE, Kuala Lumpur, Malaysia, 2018.

[24] S.-W. Luan, J.-H. Teng, D.-J. Lee, Y.-Q. Huang, and C.-L. Sung, "Charging/discharging monitoring and simulation platform for Li-ion batteries," in *TENCON 2011-2011 IEEE Region 10 Conference*, pp. 868–872, IEEE, Bali, 2011.

[25] W. Shi, J. Dong, T. B. Soeiro et al., "Design of a highly efficient 20-kW inductive power transfer system with improved misalignment performance," *IEEE Transactions on Transportation Electrification*, vol. 8, no. 2, pp. 2384–2399, 2022.

[26] Q. Ouyang, G. Xu, K. Liu, and Z. Wang, "Wireless battery charging control for electric vehicles: a user-involved approach," *IET Power Electronics*, vol. 12, no. 10, pp. 2688–2696, 2019.

[27] Y. Gao, Z. T. Ho Tse, and A. Ginart, "Analytical method for mutual inductance and optimum frequency calculation in a series-series compensated inductive power transfer system," in *2017 IEEE Applied Power Electronics Conference and Exposition (APEC)*, pp. 3720–3722, IEEE, Tampa, FL, USA, 2017.

[28] J. M. Miller, O. C. Onar, and M. Chinthavali, "Primary-side power flow control of wireless power transfer for electric vehicle charging," *IEEE Journal of Emerging and Selected Topics in Power Electronics*, vol. 3, no. 1, pp. 147–162, 2015.